

<https://doi.org/10.1038/s44385-025-00033-x>

Interstitial fluid transport dynamics predict glioblastoma invasion and progression



Cora M. Carman-Esparza^{1,2}, Caleb A. Stine¹, Naciye Atay^{1,2}, Kathryn M. Kingsmore³, Maosen Wang¹, Ryan T. Woodall⁴, Russell C. Rockne⁴, Jessica J. Cunningham¹ ✉ & Jennifer M. Munson^{1,2,5} ✉

Glioblastoma is characterized by aggressive infiltration into surrounding brain tissue, hindering complete surgical resection and contributing to poor patient outcomes. Identifying tumor-specific invasion patterns is essential for advancing our understanding of glioblastoma progression and improving surgical and radiotherapeutic strategies. Here, we leverage in vivo dynamic contrast-enhanced magnetic resonance imaging (DCE-MRI) to noninvasively quantify interstitial fluid velocity, direction, and diffusion within and around glioblastomas. We introduce a novel vector-based pathline analysis to trace downstream accumulation of fluid flow originating from the tumor core, providing a spatially explicit perspective on local flow patterns. We find that localized fluid transport metrics predict glioblastoma invasion and progression, offering a new framework to non-invasively identify high-risk regions and guide targeted treatment approaches.

Glioblastoma (GBM) is the most common malignant primary brain tumor, with a median overall survival of just 15 months following diagnosis and a 5-year survival rate of only 5%¹. Characterized by extensive infiltration into surrounding brain tissue, GBM's diffuse invasion makes complete surgical resection difficult, leaving residual tumor cells that drive inevitable recurrence and poor patient outcomes². Despite advances in clinical imaging, predicting the regions where GBM cells invade beyond the tumor bulk remains a critical challenge. Identifying areas at high risk for invasion is essential for improving surgical and radiotherapeutic planning, enabling more aggressive treatment in invasive regions and greater preservation in lower-risk areas.

Interstitial fluid flow (IFF) is an ever-present phenomenon in the brain, crucial for maintaining normal physiological functions. During tumor growth, however, IFF is altered by elevated interstitial pressures generated within the growing tumor mass³. This heightened pressure drives abnormal fluid flow across the tumor's margins. Studies in rodent GBM models have shown that surrogate tracers for IFF, such as Evans Blue dye, correspond to regions of cell invasion⁴, and mechanisms such as CXCR4-CXCL12 signaling and autologous chemotaxis have been implicated in the IFF-driven invasion process^{5,6}. While these studies offer valuable insights, they rely on invasive techniques or tissue samples and do not provide a means to quantify these dynamics in a clinically relevant, in vivo setting. There is a

pressing need for advanced, quantitative, and spatially explicit imaging metrics to link IFF to local cell invasion in patients.

Magnetic resonance imaging (MRI) is the standard imaging modality for GBM diagnosis and monitoring. Specifically, dynamic contrast-enhanced MRI (DCE-MRI) is widely used to delineate tumor boundaries based on areas of contrast enhancement, as the contrast agent leaks through the abnormal vasculature associated with GBM⁷. Current surgical resection margins are typically defined to include the contrast-enhancing tumor border and an additional 2 cm margin, an aggressive approach that disregards local spatial heterogeneities in tumor invasion. This static use of DCE-MRI ignores valuable dynamic information about how the contrast agent leaks into the parenchyma, which could provide deeper insights into the tumor microenvironment. Leveraging the Lymph4D algorithm, previously validated for analyzing fluid transport⁸, we can noninvasively quantify interstitial fluid velocity, directionality, and diffusion from DCE-MRI scans, extracting biologically meaningful metrics directly from clinical imaging.

Given the known influence of fluid flow on GBM invasion, spatially explicit patterns of interstitial fluid movement within and around tumors may correspond to regions of cell invasion. Identifying these patterns using in-vivo imaging could enable the noninvasive detection of invasive regions. In this study, we leverage quantitative analysis of DCE-MRI to examine local

¹Frail Biomedical Research Institute, Virginia Tech, Roanoke, VA, USA. ²Department of Biomedical Engineering and Mechanics, Virginia Tech, Blacksburg, VA, USA. ³Department of Biomedical Engineering, University of Virginia, Charlottesville, VA, USA. ⁴Division of Mathematical Oncology and Computational Systems Biology, City of Hope, Duarte, CA, USA. ⁵Department of Neurosurgery, Virginia Tech Carilion School of Medicine, Roanoke, VI, USA.

✉ e-mail: jcunningham@vt.edu; jm4kt@vt.edu

interstitial fluid velocity and diffusion. We introduce a novel vector-based pathline analysis to track fluid movement patterns originating from the tumor core into the surrounding brain parenchyma. To validate the predictive power of these metrics, we assess their correlation with histologically confirmed invading tumor cells and longitudinal tumor progression identified through MRI. The spatially explicit, image-based biomarkers of fluid transport dynamics presented here offer understanding of GBM invasion and progression and a significant advancement toward patient-specific treatment planning and optimization of therapeutic strategies.

Results

Fluid flow metrics are spatially heterogeneous

We performed DCE-MRI on implanted murine gliomas as described in detail in the Materials and Methods. Using Lymph4D, IFF magnitude, diffusion, and direction were calculated for each pixel within the tumor boundary and the surrounding contrast-enhancing parenchyma with measurable contrast agent. A heat map and distribution of the magnitudes for GL261 Mouse 1 shows local variation through the tumor bulk and surrounding contrast-enhancing parenchyma and highlights intra-mouse variability (Fig. 1A, B). There is also significant inter-mouse variability in both the GL261 and Glioma stem cells (GSC) mice (Fig. 1C, D). This variability is also true of the diffusion coefficient (Fig. 1E–H). Using the

directionality of flow, the trajectory of flow originating within the tumor is followed until termination (Fig. 1I). For each region in the surrounding contrast-enhancing parenchyma, the total number of tumor-originating pathlines passing through that region was summed, generating a “tumor-originating pathline density” map. This metric also exhibits significant heterogeneity of the distribution of tumor-originating fluid flow within and between mice (Fig. 1J–L).

Multimodal co-registration allows for MRI-derived flow metrics and IHC cell center analysis

Both MRI imaging and IHC sectioning were performed in the coronal plane (Fig. 2A, B). For each mouse, one or two MRI slices with the largest tumor bulk were selected (Fig. 2C). Features such as ventricles, white matter, and tumor shape were used to identify two to three corresponding histological sections for each MRI slice. Tumor boundaries were determined on both the MRI and IHC slices (Methods), and the locations of invading cells were identified (Fig. 2D). MRI and histological slices were co-registered using a multimodal registration approach (Fig. 2E, Methods), enabling the spatial coordinates of invading GL261 cells identified by IHC to be directly mapped onto the MRI images (Fig. 2F). This allowed for the integration of MRI-derived flow metrics with the precise locations of individual invading cells for spatially detailed analysis.

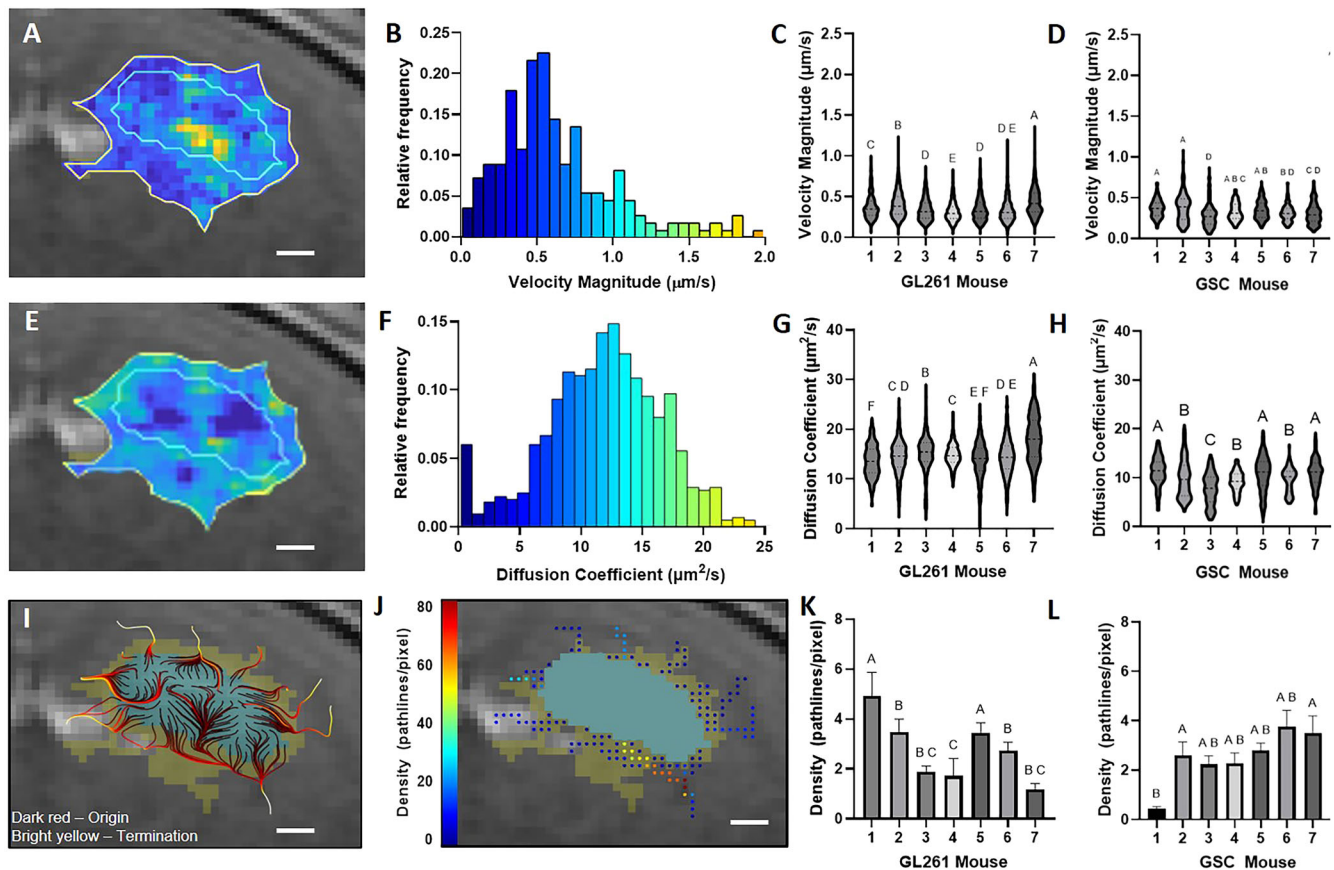


Fig. 1 | Intra- and inter-mouse variability of magnitude, diffusion, and tumor originating pathline density. **A** Heat map of tumor and surrounding contrast-enhancing parenchyma IFF magnitude ($\mu\text{m/s}$) with the tumor (blue boundary) and contrast-enhancing parenchyma (yellow boundary) (Scale bar = 500 μm). **B** Distribution of magnitudes within GL261 Mouse 1. **C** IFF magnitude of all pixels within the surrounding contrast-enhancing parenchyma for each GL261 mouse. Compact letter display shows columns are statistically indistinguishable if and only if they share at least one letter. **D** IFF magnitude of all pixels within the surrounding contrast-enhancing parenchyma for each GSC mouse. **E** Heat map of tumor and surrounding contrast-enhancing parenchyma IFF diffusion coefficient ($\mu\text{m}^2/\text{s}$) (Scale bar = 500 μm). **F** Distribution of diffusion coefficients within GL261 Mouse 1. **G** IFF diffusion coefficient of all pixels within the surrounding contrast-enhancing parenchyma for each GL261 mouse. **H** IFF diffusion coefficient of all pixels within the surrounding contrast-enhancing parenchyma for each GSC mouse. **I** Tumor-originating pathlines (dark red is initial location moving to ending location as bright yellow) (Scale bar = 500 μm). **J** Density heatmap of tumor-originating pathlines where blue and red represent a low and high tumor-originating pathline density, respectively (Scale bar = 500 μm). **K** Tumor originating pathline density of all pixels within the surrounding contrast-enhancing parenchyma for each GL261 mouse or location. **L** Tumor originating pathline density of all pixels within the surrounding contrast-enhancing parenchyma for each GSC mouse or location.

G IFF diffusion coefficient of all pixels within the surrounding contrast-enhancing parenchyma for each GL261 mouse. **H** IFF diffusion coefficient of all pixels within the surrounding contrast-enhancing parenchyma for each GSC mouse. **I** Tumor-originating pathlines (dark red is initial location moving to ending location as bright yellow) (Scale bar = 500 μm). **J** Density heatmap of tumor-originating pathlines where blue and red represent a low and high tumor-originating pathline density, respectively (Scale bar = 500 μm). **K** Tumor originating pathline density of all pixels within the surrounding contrast-enhancing parenchyma for each GL261 mouse or location. **L** Tumor originating pathline density of all pixels within the surrounding contrast-enhancing parenchyma for each GSC mouse or location.

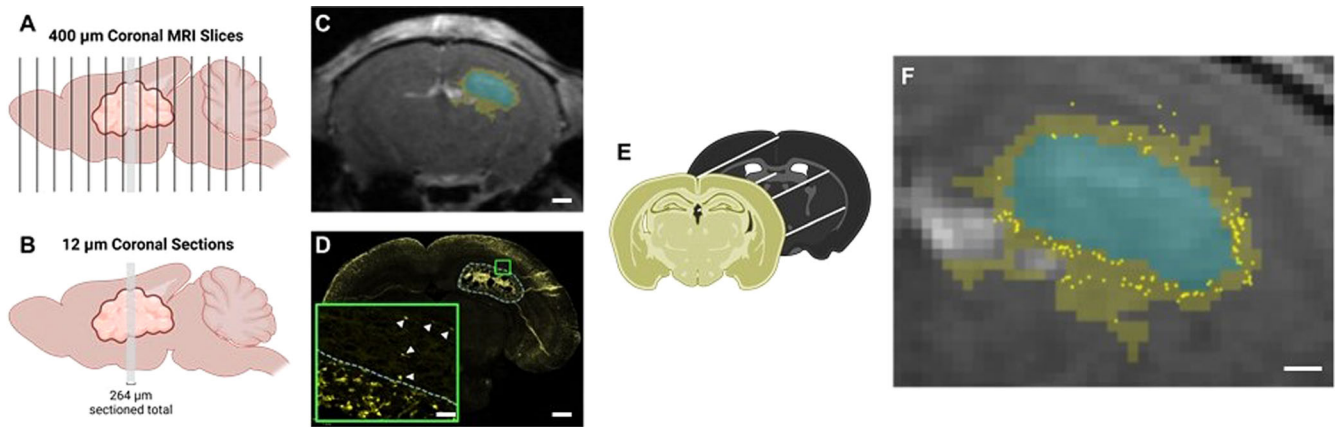


Fig. 2 | Multimodal co-registration of MRI and IHC cell centers. **A** 400 µm coronal MRI slices through the entire murine brain. **B** 12 µm IHC slices within the tumor bulk. **C** MRI slice with mass tumor bulk, with the tumor (blue) and contrast-enhanced parenchymal (yellow) regions (Scale bar = 1mm). **D** Corresponding IHC

slice with tumor boundary (Scale bar = 1mm) and inset showing individual identified invading cells (white arrows) (Scale bar = 100µm). **E** Multimodal registration using control point and geometric transformation. **F** Combined MRI features and individual invading cell locations (Scale bar = 500µm).

Average tumor velocity magnitude is positively correlated with overall invasiveness

IFF velocity magnitudes were measured in the tumor and the surrounding contrast-enhanced parenchyma of implanted GL261 tumors (Fig. 3A). The average velocity within the tumor is positively correlated with average velocity of the contrast-enhancing parenchyma (Spearman $r = 0.7509$, p value = 0.0066). The average velocity magnitude in the tumor and surrounding contrast-enhancing parenchyma for each mouse location was compared to the total number of invading cells counted in the matching histological slices for that MRI location (Fig. 3B). Velocity magnitudes in the tumor were significantly correlated with the number of invading tumor cells (Spearman $r = 0.7509$, p value = 0.0066) (Fig. 3C). The average velocity of the contrast-enhancing parenchyma and number of invading cells were not significantly correlated (Spearman $r = 0.4807$, p value = n.s.) (Fig. 3C).

Local velocity magnitude is elevated in invasive regions

The contrast-enhancing parenchymal regions that have at least one invading cell have a significantly faster velocity magnitude than regions with no invading cells; $0.47 \mu\text{m/s} \pm 0.28$ and $0.40 \mu\text{m/s} \pm 0.25$, respectively (p value < 0.001; Cohen's $D = 0.28$) (Fig. 3D). Velocity magnitude is negatively correlated with distance to boundary, meaning that in four of the seven mice higher velocities were found closer to the tumor boundary. Velocity magnitude is negatively correlated with the flow angle difference to outward normal in five of the seven mice, and positively correlated with tumor-originating pathline density, in three of the seven mice, showing that regions with elevated velocities were found where flow was directed away from the tumor boundary. Additionally, velocity magnitude is positively correlated with diffusion and invasive cells in three mice (Fig. 3E).

Local diffusion coefficient is lower in invasive regions

Diffusion coefficients were measured in the tumor and surrounding contrast-enhancing parenchyma of implanted GL261 tumors (Mouse 1 shown) (Fig. 4A). The average diffusion coefficient in the tumor and the contrast-enhanced parenchyma were significantly correlated (Supplementary Fig. 5). The average diffusion coefficient in the tumor and surrounding contrast-enhancing parenchyma for each mouse location was compared to the total number of invading cells counted in matching histological slices for that MRI location (Fig. 4B), but these were not significantly correlated (Fig. 4C). More importantly, when the spatially local diffusion coefficients were analyzed, as opposed to the overall bulk averages, regions that have at least one invading cell do have a significantly lower diffusion coefficient than regions with no invading cells (11.59 ± 5.73 vs. 13.87 ± 4.96 (p value = <0.001; Cohen's $D = 0.43$) (Fig. 4D). This underscores the importance of considering the spatial heterogeneity of transport metrics and focusing on

individual local regions rather than relying on overall averages. The diffusion coefficient is positively correlated with the distance to boundary for five of the seven mice, meaning that for each of these mice, the diffusion coefficient increases as the distance from the tumor increases (Fig. 4E). There are only sparse significant correlations of diffusion with other IFF metrics across the mice, though five of the seven mice had significant negative correlation to invasion, which highlights that regions with invading cells have lower diffusion coefficients across the majority of the mice.

Tumor-originating fluid flow is significantly elevated in regions of invasion

The tumor-originating pathline density metric represents the relative amount of fluid originating from the tumor that traverses a given local region, with a higher pathline density indicating a greater volume of tumor-derived fluid passing through that parenchymal area. In Mouse 1, the tumor pathline density and histologically identified invading cells are shown (Fig. 5A–C). Tumor-originating pathline density is significantly higher in local regions that have at least one invading cell (2.35 ± 7.54 vs. 5.55 ± 11.31 (p value < 0.001; Cohen's $D = 0.33$) (Fig. 5D). This demonstrates that regions experiencing outward fluid flow from the tumor bulk into the parenchyma have significantly more invading cells, as quantified by this novel metric. Overall, we found that tumor originating pathlines intersected with 40–89% of all invading cells within each mouse with an average across all mice of 60.14% of invading cells (Fig. 5E).

In all seven mice, tumor-originating pathline density was negatively correlated with distance to the boundary, as expected, as all pathlines originate within the tumor, and the density of outward flow naturally diminishes with increasing distance from the tumor. In three mice, there was a positive correlation with velocity magnitude meaning in these mice, regions with higher levels of tumor originating flow passing through them also experience higher velocity magnitudes. In all seven mice, outward flow is significantly correlated with invasion. Observing this pattern consistently across all mice in the study underscores the predictive power of this novel metric in identifying regions of invasion.

Transport metrics significantly correlated with MRI-identified progressive disease

While identifying individual invading cells provides localized insights, radiographic progression reflects broader tumor growth dynamics. Here, we analyze the underlying transport metrics associated not with individual cell invasion but with radiographic progression using a patient-derived xenograft (PDX) (G34) as a more representative model of human disease than the GL261 syngeneic tumor model. For Mouse P1, the tumor boundary on Day 6 post injection (Fig. 6A) and the tumor boundary on Day 8 post

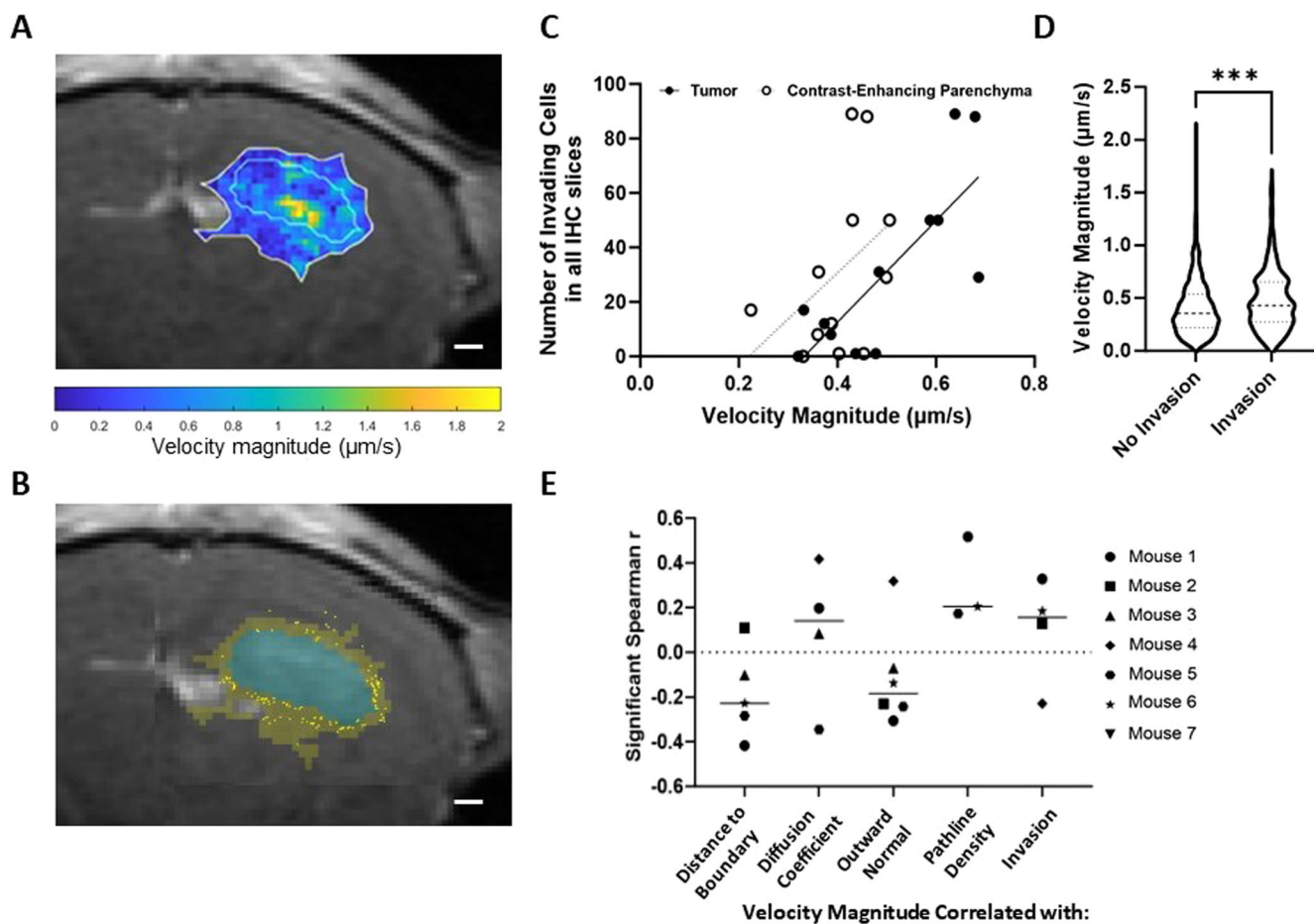


Fig. 3 | Increased velocity magnitude is associated with elevated invasion.

A Heatmap of velocity magnitude with tumor and contrast-enhancing parenchyma in light blue and yellow outlines, respectively (Scale bar = 500 μm). **B** Invasive cells (yellow points) overlaid on MRI (Scale bar = 500 μm). **C** Correlation of total number of invading cells and average velocity magnitude within the tumor (Spearman $r = 0.7509$, p value = 0.0066) and contrast-enhancing parenchyma (Spearman $r = 0.4807$, p value = n.s.) for all MRI slices examined. **D** Velocity magnitude in each

injection (Fig. 6B) are shown. Creating a difference map between Day 8 and Day 6 highlights the pixels corresponding to areas of radiographic progression (purple highlight) with contrast-enhanced parenchyma (yellow) (Fig. 6C). The tumor-originating pathline densities from the fluid flow measured on Day 6 are shown (Fig. 6D, Supplementary Dataset 2). We found that regions containing progression by Day 8 had a significantly faster velocity magnitude on Day 6 than regions that did not show progression (p value = 0.0093; Cohen's $D = 0.15$) (Fig. 6E). Additionally, regions containing progression by Day 8 had a significantly lower diffusion coefficient on Day 6 than regions that did not show progression (p value < 0.001; Cohen's $D = 0.26$) (Fig. 6F, Supplementary Fig. 3). Further, tumor-originating pathline density was significantly higher in regions that exhibited progression (p value < 0.001; Cohen's $D = 0.31$) (Fig. 6G).

Both histological invasion and radiographic progression are captured by the same transport patterns

The observed correlations between transport metrics and the spatial radiologic progression mirror the correlations identified in the study where invasion was quantitatively assessed using histological tissue sections (Fig. 6H, I). Regions of progression and invasion were negatively correlated with distance to boundary, meaning both are occurring close to the tumor boundary, as expected. Regions of progression and invasion were negatively correlated with the diffusion coefficient in four and five of the seven mice,

region with and without at least one invading tumor cell (Mann-Whitney U test performed, p value < 0.001; Cohen's $D = 0.28$; no invasion ($N = 2402$); invasion ($N = 208$)). **E** Multiparametric correlation analysis of local velocity magnitudes and each flow parameter. All correlations shown are significant as obtained from a Spearman correlation. Each point represents one of seven mice; missing points indicate mice without significant values for that parameter.

respectively. Tumor-originating pathline density was positively correlated with progression in three of the seven mice and with invasion in all seven mice, indicating regions with increased tumor-originating outward flow can be associated with both progression of disease and invasion. These results indicate that transport metrics can characterize single-cell invasion at a given time point while also capturing the broader, cumulative impact of such invasion on disease progression.

Discussion

In this study, we developed a set of analytical techniques to quantify transport metrics of IFF as determined by non-invasive MR imaging and link those metrics to important physiological outcomes (Table 1). We have previously validated the use of DCE-MRI for measuring transport within and around glioma based on underlying physical principles⁹. Our features include distance from delineated tumor boundary, fluid flow velocity, diffusion coefficient, and two novel metrics to quantify fluid moving with respect to the tumor boundary: angle difference of tumor boundary normal vector to fluid flow direction and density of tumor-originating pathlines. We directly linked these transport features to GBM invasion and progression in mice.

Specifically, averages of tumor-wide velocity magnitude as well as spatially explicit local analysis of velocity magnitude reveal a positive correlation with invasion. Interestingly, overall averages of diffusion coefficient

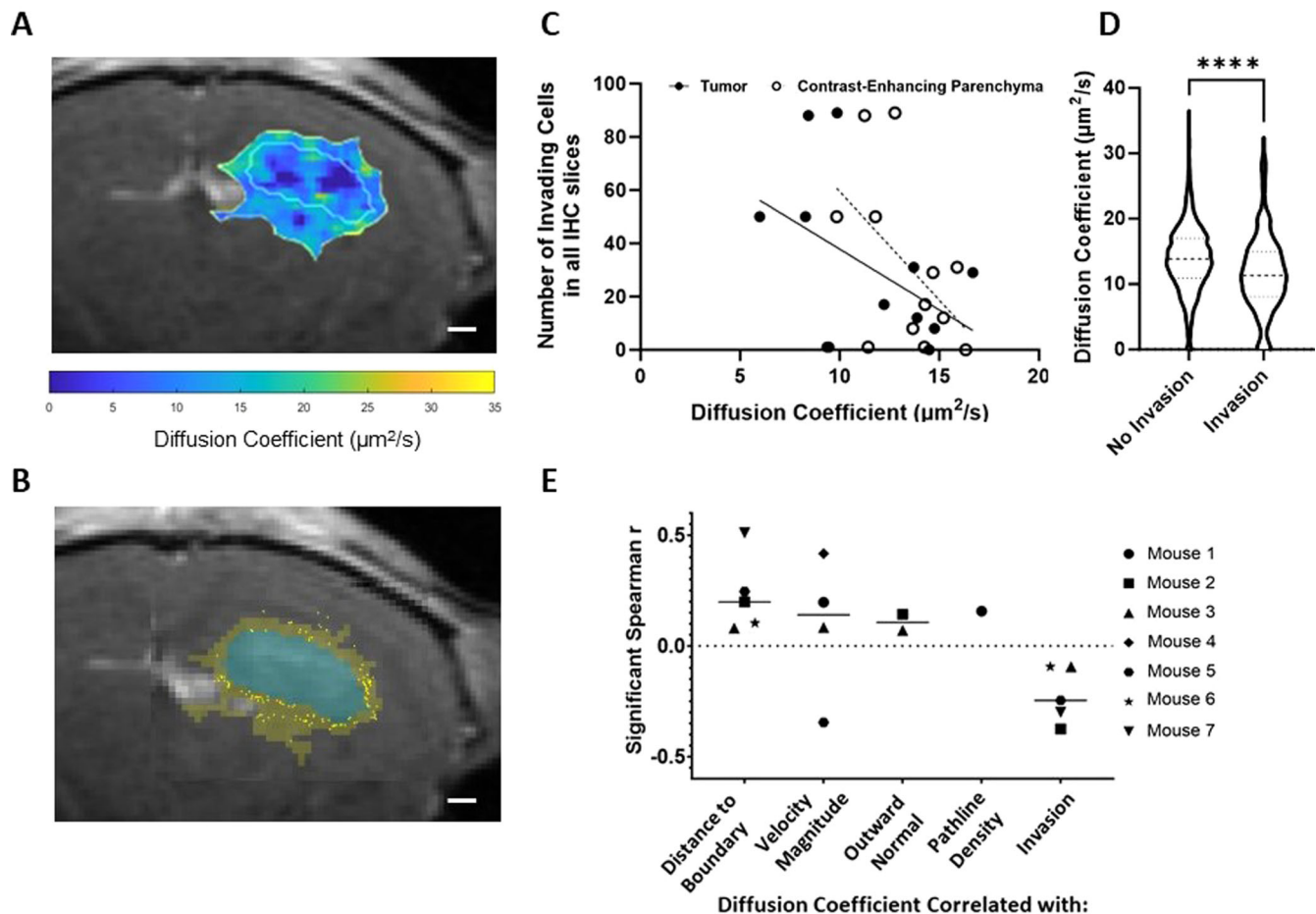


Fig. 4 | Decreased diffusion is associated with invasion. **A** Representative heatmap of diffusion coefficient indicating the tumor and surrounding contrast-enhancing parenchyma in blue and yellow outlines, respectively (Scale bar = 500 μm). **B** Invasive cells (yellow points) overlaid on MRI highlighting the tumor (blue) and contrast-enhanced parenchymal (yellow) regions (Scale bar = 500 μm). **C** Average diffusion coefficient of the tumor and surrounding contrast-enhancing parenchyma is not significantly correlated with the number of invasive cells counted, though there is a negative trend (Tumor: Spearman $r = -0.4351$, p value = n.s.; Contrast-

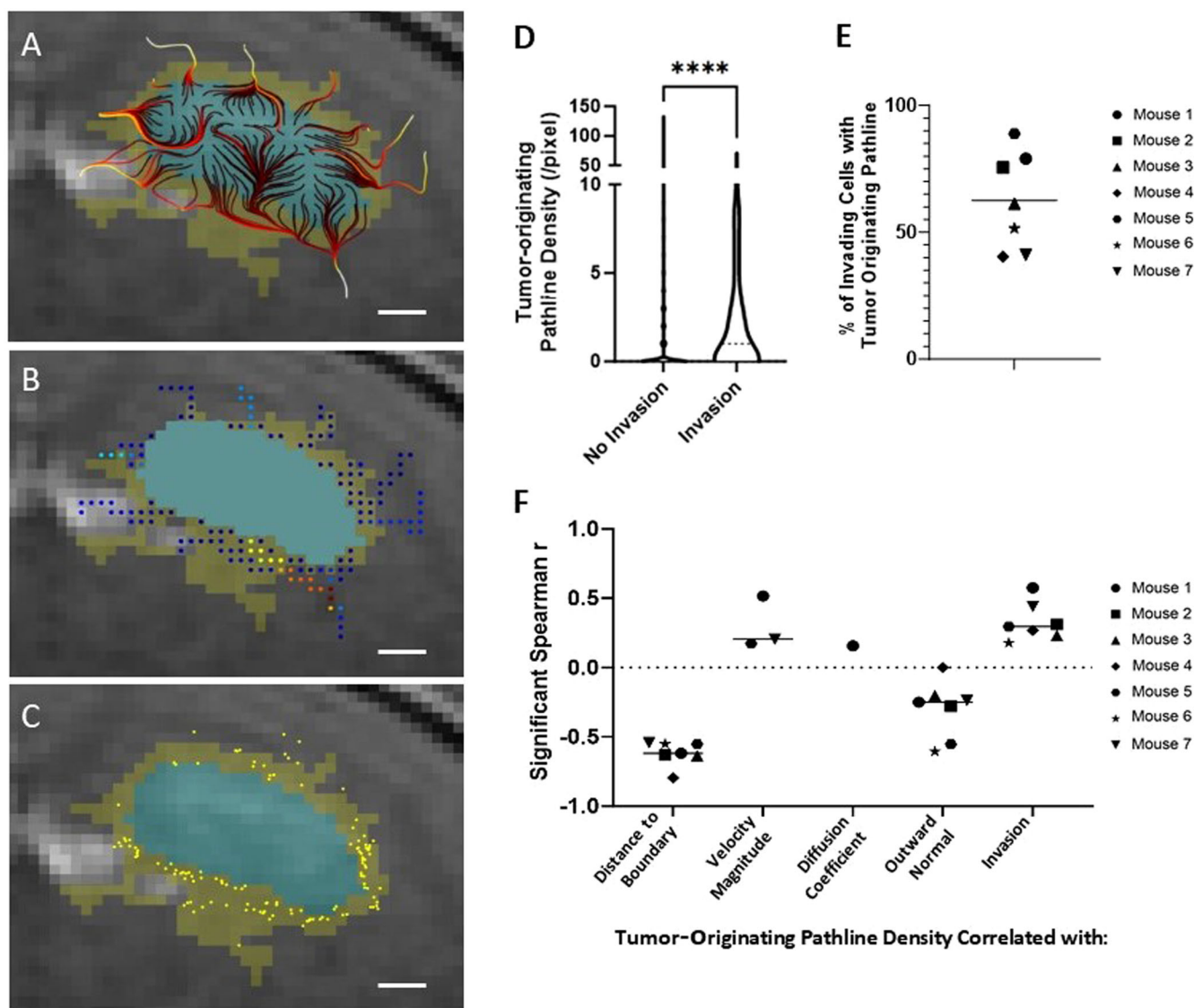
enhancing parenchyma: Spearman $r = -0.4737$, p value = n.s.). **D** The diffusion coefficient in each local region with at least one invading tumor cell is significantly lower than regions without invasion (Mann-Whitney U test performed, p value = <0.001 ; Cohen's $D = 0.43$; No Invasion ($N = 2402$) Invasion ($N = 208$)). **E** Multiparametric correlation analysis of diffusion coefficient. All correlations shown are significant (p value < 0.05) as obtained from a Spearman correlation. Each point represents one of seven mice; missing points indicate mice without significant values for that parameter.

exhibit no correlation to invasion, but the diffusion coefficient does have a significant negative correlation to invasion when interrogated at a finer spatial resolution in some mice. Notably, tumor-originating pathline density emerges as a novel transport metric associated with invasion that correlated in all of the tumors examined. These transport metrics that significantly correlate with histologically identified invading cells are the same metrics that correlate with radiographic progression in our PDX.

Elevated velocities have been implicated in a host of cancers, primarily breast and glioma^{10–13}. Application of elevated velocities on tumor cells has been linked to increased glioma cell invasion *in vitro*¹⁴ and *in vivo*⁶. We and others have identified underlying mechanisms that drive flow-induced glioma invasion consisting of both intra- and extracellular drivers¹⁵. Of interest to the current study, when cells are exposed to subtle IFF, pericellular gradients of CXCL12 can drive directional migration through autologous chemotaxis¹⁶. These gradients, as modeled *in silico*, are sensitive to the features of flow, including magnitudes and directionalities, indicating a potential sensitivity to the complex flows that we see through our image analysis¹⁷. *In silico* models have explored these complex flow patterns that arise due to contributions of the tumor microenvironment, such as heterogeneous vasculature and intratumoral pressure^{18,19}. Seminal work investigating transport in glioma reports intratumoral pressures drive interstitial flow into the surrounding parenchyma, though the heterogeneity

of flow within and around tumors in the brain remained understudied in experimental models^{20,21}. Our localized analysis shows that heterogeneity of fluid flow transport within and around the tumor differentially accounts for spatially varying invasion patterns. Thus, considering local transport trends is important to better understand initial invasion and ultimate progression of the disease.

The diffusion coefficient within cancer tissue has been associated with both the presence and progression of disease. In endometrial, cervical, and breast cancers, diffusion coefficients are typically lower than in corresponding healthy tissues^{22–25}. One retrospective clinical study in patients with GBM interrogated all voxels as individual data points and, similar to our study, found that regions of progression were most associated with a lower apparent diffusion coefficient²⁶. One marked difference between our results and these reports is that we measure the apparent diffusion coefficient of the contrast agent gadolinium through the solution of the mass transport equation. Other studies use the apparent diffusion coefficient of water based on diffusion tensor imaging MRI. As the diffusion coefficient is directly related to molecule size, it follows that our calculated rates are slower than these reported rates, due to the difference in size between water and gadolinium. The biological reasons for this relationship are not fully known, as there are seemingly counteracting elements involved. Specifically, diffusion can be limited in denser matrices, with reduced porosity, and thus, cells



may have more limited free movement. However, these denser matrices offer binding sites of preferential interactions with receptors on tumor cells that could have an inverse effect on more active motility^{27–29}. Other effects specific to diffusion coefficient relate to the interactions between the substrate measured and the surrounding tissue, such as electrostatic charge, which may also be interacting with cells in interesting ways for further exploration.

As invasion ultimately originates from the tumor bulk and travels into the parenchyma, the ability to examine and quantify downstream implications of tumor cell phenotypic changes and of tumor-associated drainage is important. The density of tumor-originating pathlines in the parenchyma offers knowledge not only about the tumor but also about how the tumor interfaces with the surrounding tissue in order to identify regions of interest for further analysis. Regions of elevated pathline accumulation may be where interstitial flow from the tumor converges before entering drainage

pathways. Vasculature may serve as conduits for gadolinium drainage, specifically funneling into perivascular spaces known for the transport of fluid through the parenchyma³⁰. Perivascular invasion is a hallmark of GBM and thus, could be a linking factor between the flow pathways and invasion seen in our correlative analysis.

Elevated flow may affect individual cell types or potentially confer phenotypic changes to the cells. We know that CXCR4/CXCL12 is an important pathway in glioma cells that are responsive to IFF as documented in vitro and in vivo^{5,6,9}. Similarly, CD44 as the hyaluronic acid receptor, has also been implicated in the invasion of tumor cells in response to flow^{9,14}. Both of these molecular markers are important for various phenotypes in GBM that contribute to malignancy of disease including progression and histopathological grade^{31,32}. The CXCR4/CXCL12 signaling cascade has also been implicated in temozolomide resistance³³. CD44+ tumor cells, classified as being more of a mesenchymal subtype, have been shown to have

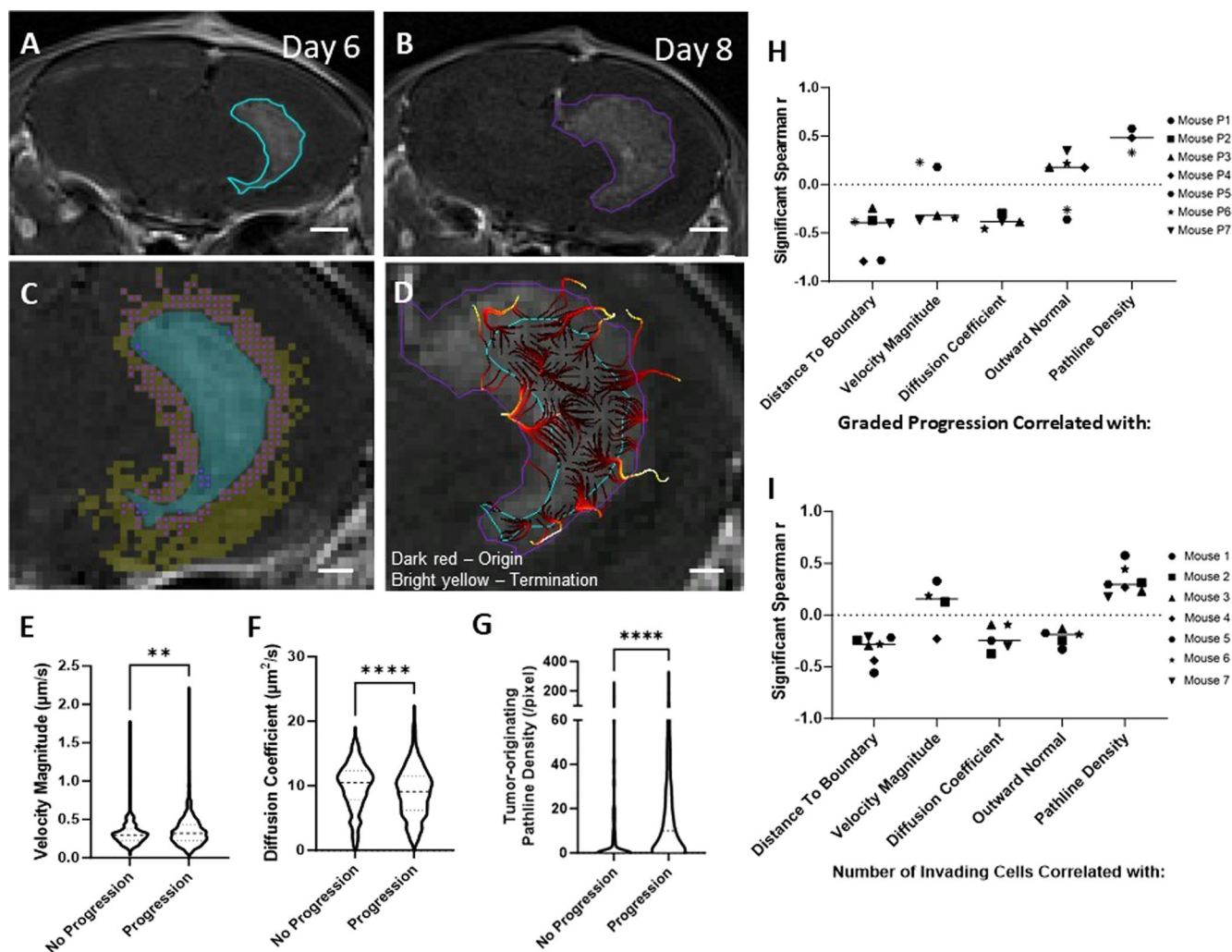


Fig. 6 | MRI-identified glioma progression correlates with diffusion coefficient, pathlines, and velocity magnitude in a patient-derived xenograft model. **A** Day 6 tumor boundary (cyan) as identified on T1 image (Scale bar = 1 mm). **B** Day 8 tumor boundary (purple) as identified on a T1 image in the same tumor (Scale bar = 1 mm). **C** Pixels containing tumor on Day 8 (purple points) within the contrast-enhancing parenchyma of Day 6 (yellow pixels) are classified as “Progression,” whereas all remaining contrast-enhancing pixels in the parenchyma are classified as “No Progression” (Scale bar = 500 μm). **D** Day 8 MRI is overlaid with Day 8 tumor boundary (purple), Day 6 tumor boundary (cyan) and Day 6 tumor-originating pathlines (dark red to yellow transition indicates direction of pathline origination to termination) (Scale bar = 500 μm). **E** Local velocity magnitude comparison between no

progression and progression regions (Mann-Whitney U test performed, p value = 0.009; Cohen’s D = 0.15; No Progression (N = 435) Progression (N = 1524)). **F** Local diffusion coefficient comparison between no progression and progression regions (Mann-Whitney U test performed, p value < 0.001; Cohen’s D = 0.26). **G** Tumor originating pathline density comparison between no progression and progression regions (Mann-Whitney U test performed, p -value < 0.001; Cohen’s D = 0.31). **H** Neighborhood multiparametric correlation analysis of MR-signal identified graded progression metric. **I** Neighborhood multiparametric correlation analysis of histologically identified invasion. All shown correlations are significant based on Spearman analysis. Each point represents one of seven mice; missing points indicate mice without significant values for that parameter.

higher resistance to radiation therapy^{31,34}. Interestingly, they are also more associated with other known players in microenvironmentally-conferred treatment resistance, such as hypoxic regions or perivascular niches^{35–37}. By coupling our flow-based approaches with other spatial profiling methods for tumor cell and tumor microenvironment markers, we can explore the unique changes to regions showing higher exposures to interstitial flow.

The primary aim of the methodology developed here is to apply it to clinical images to gain spatial insight into recurrence and tumor margins in glioma patients. Invasive tumor margins in GBM yield incomplete resection, therapeutic targeting, and, ultimately, recurrence in patients. Thus, the ability to utilize non-invasive standard of care imaging and quantitative metrics like those developed in this study to aid in the identification of tumor cells at these margins has long been sought³⁸. Intraoperative identification of tumor cells has been achieved using imaging agents, such as 5-ALA³⁹ and the field of photodynamic therapies is rapidly growing to incorporate improved imaging agents⁴⁰, though these methods are limited to surface identification

during surgery, and do not describe deeper tissue invasion beyond 3–5 mm or progression⁴¹. Methods to leverage MRI combined with AI or machine learning have been probed to define treatment margins or predict progressive disease⁴², yet few are grounded in the inherent underlying physical and biological drivers of tumor invasion, like fluid transport and interstitial flow-increased invasion. Labeling glioma cells with iron-oxide nanoparticles enables tracking of progression along specific structures⁴³, however, cell-labeling methods lack translatability to patients and are detection limited. While translating the quantitative approach presented here to clinical imaging presents several challenges, it remains feasible with current and emerging techniques. Registration across sessions is more complex in the clinical setting due to factors such as variability in scan acquisition across sites (e.g., emergency room vs. post-operative imaging). Post-surgical brain shift presents a major challenge for accurate registration in clinical imaging, though emerging approaches using deformable registration with masking offer solutions⁴⁴. Of note, clinically standard DCE imaging successfully

Table 1 | Summary of key dynamics between IFF parameters and glioma cell invasion in murine models

Transport Metric	Cell invasion and radiographic progression
Velocity Magnitude	Increased
Diffusion Coefficient	Decreased
Tumor-Originating Pathline Density	Increased

captures early contrast dynamics, providing a potential opportunity for adapting the present analysis methods to work within clinical constraints.

While we have presented novel quantitative metrics from DCE-MRI, they should not be relied upon in isolation. Our fluid flow metrics can and should be added to the feature space that can be obtained from other MR imaging modalities. Some MRI-calculated features that have been clinically correlated with survival in glioma include: preoperative tumor volume, Karnofsky performance status, tumor location, edema, extent of resection, contrast enhancement, temporal changes in serum proteomics and pH^{45–49}. Specifically, perfusion imaging has been one of the most clinically used MRI scans in the treatment of glioma, providing vessel leakiness from $K_{T_{trans}}$ to identify specific biomarkers indicative of progression and recurrence^{50,51}. These perfusion metrics have also been found to be predictive of tumor grade and treatment response³⁸. Combining our novel features with these existing metrics offers a promising approach to improve the accuracy of tumor margin delineation and understanding disease dynamics. For instance, combining these features using more advanced modeling techniques (e.g., linear and non-linear combination classifiers) may yield better performance compared to relying on individual metrics alone.

In conclusion, our study presents a significant stride towards non-invasive, in vivo localization of invading tumor cells through the development of quantitative metrics of IFF derived from DCE-MRI. This advancement not only offers the potential to identify additional mechanisms and correlates of invasion via complementary tissue-level analyses such as immunohistochemistry (IHC) but also opens avenues for exploring extracellular matrix components, metabolites, and cellular reactivities relevant to glioma invasion⁵². Furthermore, a deeper understanding of transport parameters in and around invasive regions holds promise for the development of targeted therapeutic delivery strategies that leverage the unique transport characteristics of these areas. These metrics could support a shift away from uniform 2 cm surgical margins and more personalized radiation approaches, potentially sparing healthy brain tissue, reducing treatment-related morbidity and toxicity, and concentrating therapy where it is most needed. Ultimately, this study presents a first step towards the promise of translating IFF analyses into tangible improvements in patient outcomes.

Methods

Cell culture

GL261-GFP cells were generated as previously described in ref. 12. Cells were maintained for at least three passages after thawing with Dulbecco's Modified Eagle Medium (DMEM) + 10% fetal bovine serum (ThermoFisher, Gibco). Cells were resuspended at a concentration of 20,000 cells/uL in serum-free media for tumor implantation as described previously⁶. GSCs G34, a generous gift from BJ Purow at the University of Virginia, were cultured following the previously described protocol in ref. 53. GSCs were cultured in neurobasal media (ThermoFisher) with N2 and B27 without vitamin A supplements (ThermoFisher), human recombinant basic fibroblast growth factor and epidermal growth factor (50 ng mL⁻¹, ThermoFisher), Glutamax (ThermoFisher), and Penicillin–Streptomycin (ThermoFisher) in low-adhesion tissue culture flasks (Grenier).

In vivo tumor model

Invasion-flow correlation study. For GFP-GL261 injections, all animal procedures were approved by the Institutional Animal Care and Use

Committee at Virginia Polytechnic Institute and State University under approved protocol #20-146. Ten, 8–11-month-old transgenic B6.Cg-S1pr3tm1.1Hrose/J mice⁵⁴ (JAX stock #028624) were anesthetized with isoflurane and connected to a stereotactic frame. A burr hole was drilled at coordinates $-2, +2, -2.2$ (AP, ML, DV) from bregma, and 100,000 GFP + GL261 cells in 5 μ L serum free DMEM were injected via a Hamilton syringe and syringe pump (World Precision Instruments) at 1 μ L/min for 5 min. The syringe was inserted to a depth of 3 mm then retracted 0.5 mm before injection. The Hamilton syringe was removed three minutes after the completion of the injection to prevent reflux, and the burr hole was sealed with bone wax.

PDX progression study. The progression study was conducted at the University of Virginia under approved protocol 4021. Seven 8–10-week-old SCID mice were injected using the same protocol as previously published in ref. 9. Mice were injected with G34 GSCs, and the tumors were allowed to grow for 10 days. T1, T2, and DCE-MRI imaging were performed on days 6, 8, and 10. Following DCE-MRI, mice were euthanized via cardiac perfusion, and brains were harvested.

Magnetic resonance imaging

Invasion-flow correlation study. DCE-MRI was performed on all mice with detectable tumors on Days 15 and 24 to allow for tumor growth. Mice were imaged with a 9.4 T small animal MRI (Bruker BioSpec AVANCE NEO 94/20 USR, Ettlingen, Germany) equipped with 660 mT/m high power gradient. An active detunable 86 mm volume coil was used as the transmit coil, and a planar 20 mm receive-only surface coil was used as the receive coil. A T2-weighted image was taken using rapid acquisition with relaxation enhancement (RARE) sequence to confirm tumor growth with the following parameters: repetition time (TR) = 1800 ms, echo time (TE) = 40 ms, field of view (FOV) = 19.2 \times 19.2 mm with a 192 \times 192 matrix, slice thickness = 0.5 mm, number of slices = 16, with nine averages requiring a total acquisition time of about 6.5 min per mouse.

To measure the interstitial fluid transport metrics, a pre-contrast T1-weighted image was collected followed by tail vein injection of Gadolinium (Magnevist, Bayer HealthCare Pharmaceuticals) at a concentration of 0.1 mmol/kg in sterile, heparinized saline. Four post-contrast T1-weighted images were acquired for approximately 12 min post-injection, as previously published⁴. T1-weighted images were acquired using a fast low angle shot sequence using the following parameters: repetition time (TR) = 180 ms, echo time (TE) = 11 ms, FOV = 19.2 \times 19.2 mm with a 192 \times 192 matrix, slice thickness = 0.5 mm, number of slices = 16, and 7 averages requiring a total acquisition time of about 3 min per sequence (Supplementary Fig. 1).

Progression Study. For GSC-injected mice, DCE-MRI was performed on days 6, 8, and 10 according to the protocol established in prior publications^{4,9}. These earlier time points, compared to day 15 for the GL261 model, were chosen to match tumor size across models, accounting for differences in in vivo growth rates among glioma stem cell lines. This timing allowed for more consistent comparisons of tumor behavior and imaging metrics despite biological variability.

Tissue harvest, cryosectioning, IHC, and microscopy

Mice were euthanized and transcardially perfused with ice cold 1 \times phosphate buffered saline followed by 4% paraformaldehyde (PFA). Brains were post-fixed in PFA for 18 h and placed in 30% sucrose until complete submersion was achieved. Afterwards, brains were placed in molds of optical cutting temperature compound at -80°C and sectioned at 12 μ m thickness on a cryostat. Specific MRI slices of interest were identified on T2-weighted MRI based on tumor size and minimal needle-track damage. One to two distinct MRI tumor locations were sectioned per mouse. Structural features (i.e., ventricles, white matter, tumor shape) in the T2-weighted MRI images were used as a guide during cryosectioning to collect cryosectioned slices corresponding to the identified MRI slice of interest. At each location, two to three histological sections were used for the analysis based on tissue quality

(Supplementary Fig. 2). Slides were stained with DAPI (ThermoFisher) for 10 min and imaged at 20X on a VS200 Olympus Slide Scanner with DAPI in the blue channel and GFP + GL261 cells in the green channel.

Registration of histological tissue sections to MRI slices

Control point image registration was performed in MATLAB. A local weighted mean geometric transformation was used to account for orientation and shape differences between the MRI slices and the histological tissue section. At least 12 distinct, reliable anatomical landmarks in both the MRI and histological tissue sections were chosen for each registration. Registration control points were selected on consistent gross anatomical features such as the brain shape and ventricles, minimizing any impact of modality differences. IHC-identified spatial coordinates of the invading GL261 cells and vertices of the tumor boundaries were registered to the MRI using the resulting transformation matrix. A composite tumor boundary was created for each MRI image that preserves only areas identified as tumor bulk in all histological technical replicates (Supplementary Fig. 3).

Identification of tumor boundary and invading tumor cells

The DAPI and GFP channels were split and exported individually using ImageJ. The green channel of the GFP + GL261 cells were thresholded based on intensity to remove background fluorescence. Images were colocalized with DAPI staining to include only the GFP signal associated with a nucleus (DAPI). ImageJ watershed segmentation was used to separate touching or overlapping nuclei. The resulting identified objects represented individual GL261 cells.

To identify invading tumor cells and define the boundary between these cells and the main tumor bulk, we used a combination of manual and computational methods. Invading cells were defined as any GL261 cell located outside the contiguous tumor mass and were manually identified (Supplementary Fig. 4). To improve the accuracy and reliability of this manual classification, two independent investigators jointly reviewed each histological section and labeled each GL261 cell as either bulk or invading. This process was carried out across multiple serial IHC sections from the same MRI slice, which served as technical replicates and increased confidence that no invasive region was completely missed, and that regions identified as invading reflected true invasion.

The boundary of the remaining contiguous tumor bulk, meaning the GL261 cells not marked as invading, was then defined using a computational approach. The (x, y) coordinates of these cells were input into the MATLAB boundary function, which generated a polygon that enclosed the main tumor area and returned a set of (x, y) vertices outlining the tumor border. This IHC-defined tumor boundary, after registration to MRI, is used as the MRI tumor boundary.

Transport metric analysis

From the DCE-MRI sequence, transport metrics were obtained using “Lymph4D,” a previously published and openly available tool⁸. Briefly, parameter optimization is performed in a pixel-wise manner for the two-dimensional diffusion-advection equation to identify the combination of the velocity magnitude and direction of advection and diffusion coefficient that best describes the change in gadolinium over time of that pixel acquired by the DCE-MRI.

Defining the contrast-enhancing parenchymal region

To ensure that transport metrics were obtained in pixels that experienced influx of gadolinium, we developed a strategy to define these regions. To determine whether a pixel experienced gadolinium signal, we used an analysis of the standard deviation (SD) of the time-signal intensity curve (TSIC) of each pixel. The SD of the TSIC for each pixel is calculated using the following formula:

$$SD_{\text{pixel}} = \sqrt{\frac{1}{N} \sum_{i=1}^N (I(t_i) - \bar{I})^2}$$

where N is the number of time points in the DCE-MRI, $I(t_i)$ is the intensity of the pixel at time t_i , and \bar{I} is the mean intensity of the TSIC of that pixel over all time points. To identify contrast enhancement at the pixel level, we compared the SD_{pixel} of each pixel to the mean SD_{pixel} of an ROI in the contralateral brain, which served as the noise baseline. We considered a pixel to be contrast-enhancing if its SD_{pixel} exceeded two SD above the mean SD of the contralateral noise ROI. This thresholding approach enabled the delineation of regions exhibiting contrast enhancement. Within these regions, transport metrics computed using Lymph4D were deemed reliable and above the noise threshold.

The result was a semi-automatically identified region of contrast-enhanced parenchyma where the transport metrics calculated using Lymph4D were considered valid and not noise (Supplementary Fig. 4).

Definition of outward flow metrics

Flow normal to boundary is defined as the difference between the IFF direction vector at each pixel and the normal vector at the nearest point on the tumor boundary. For a given pixel, the closest point to the tumor boundary was identified by finding the boundary vertex with the minimum Euclidean distance to the center of the pixel. To calculate the normal vector at this boundary vertex, two lines extending out from this boundary vertex were identified using the two adjacent boundary vertices. The normal vectors of these lines are the perpendicular lines that point away from the tumor bulk. The average direction of these two normal vectors was weighted by the distance away from the boundary vertex of interest to give a more accurate estimate of the normal vector at the boundary vertex of interest. The flow difference to the outward normal metric was calculated by taking the angle difference between the IFF direction vector and the boundary normal vector. This metric has a value between [0, 180], where zero indicates an IFF flow pointing directly away from the tumor boundary and 180 indicates an IFF flow direction pointing directly toward the tumor boundary.

Tumor-originating pathlines were obtained by tracking the trajectories of virtual particles with origination points within the tumor boundary. A pathline is obtained by seeding a particle at a location given by $\vec{s}(t_0) = (x_0, y_0)$ within the MRI image. The virtual particle seeded at this location will have a velocity given by $\vec{u}_{\text{particle}}(t_0) = \vec{u}(x_0, y_0)$ where u is defined by the velocity of the flow field provided by DCE-MRI analysis. The particle trajectory $s_{\text{particle}}(t)$ is calculated using ODE45 in MATLAB. This method places a particle at the center of each pixel contained within the previously calculated tumor boundary and calculates the trajectory until termination, meaning it reaches a velocity equal to zero. For a given pixel, the number of tumor-originating pathlines that traverse the pixel is summed and reported as the “tumor-originating pathline density” (Supplementary Fig. 6).

Tumor- and contrast-enhanced parenchymal-wide analysis

Each transport metric was averaged for the overall tumor area and for the contrast-enhanced parenchymal region. *Statistical analysis:* Unpaired Mann-Whitney U tests and Spearman r correlations were used to compare averaged tumor and contrast-enhanced parenchymal transport metrics.

Local metric analysis

For each pixel within the tumor boundary and the identified contrast-enhanced parenchyma, a feature vector was constructed including the following metrics: distance to boundary, flow magnitude, diffusion coefficient, flow direction angle difference to boundary normal, tumor-originating pathline density, and number of invading cells. The distance to boundary metric is calculated as the Euclidean distance between the focal center of the pixel and the nearest point on the tumor boundary. The flow magnitude, diffusion coefficient, and flow direction angle difference to outward normal are calculated by averaging this value of each metric in the 3×3 pixel neighborhood surrounding the pixel. For the tumor-originating pathline density and the number of invading cells, the values of these metrics in all nine individual pixels in the 3×3 pixel neighborhood are summed (Supplementary Dataset 1). *Statistical analysis:* Unpaired Mann-Whitney t-tests

were used to compare transport metrics in pixels with and without invasion. Pearson r correlations were used for multiparametric correlation analysis. Cohen's d was calculated to report effect sizes, providing a standardized measure of the magnitude of differences between groups.

Progression analysis on tumor growth differences

For each mouse, a T1-weighted MRI slice of interest was manually identified that included the largest tumor area observed six days post-tumor injection. IFF transport metrics were calculated, and contrast-enhanced parenchyma was identified using the DCE-MRI of this slice of interest. Manual slice matching of T2-weighted images to the DCE-MRI modality was required for tumor segmentation. Manual slice matching was performed by concurrently comparing the lesion and surrounding anatomy between the DCE-MRI and T2-weighted images from both six- and eight-day post-injection. Anatomically matched T2-weighted images from six- and eight-day post-injection were registered to the T1-weighted slice of interest using control point registration with a nonreflective similarity transformation in MATLAB. Waypoints were selected based on consistent anatomical landmarks, including the ventricles and skull, which remain clearly identifiable across both T1- and T2-weighted images (Supplementary Dataset 2). On these registered T2-weighted images, the tumor was manually segmented, and the regions segmented as tumor eight days post injection that were not segmented as tumor six days post injection were identified as tumor progression. Any pixel on the T1-weighted slice of interest, including any part of this identified progression region, was classified as a progression pixel. "Graded progression" is defined as the number of pixels in the 3×3 pixel neighborhood classified as progression, with possible values from [0,9]. **Statistical analysis:** Unpaired Mann-Whitney t -tests were used to compare transport metrics in pixels with and without progression. Pearson r correlations were used for multiparametric correlation analysis. Cohen's d was calculated to report effect sizes, providing a standardized measure of the magnitude of differences between groups.

Data Availability

Data is available on request and not appropriate for deposit in a repository.

Code availability

Code is available on github (Lymph4D: <https://github.com/avaccari/Lymph4D/blob/main/lineCreate.m>).

Received: 21 March 2025; Accepted: 25 June 2025;

Published online: 03 September 2025

References

- Delgado-López, P. D. & Corrales-García, E. M. Survival in glioblastoma: a review on the impact of treatment modalities. *Clin. Transl. Oncol.* **18**, 1062–1071 (2016).
- Seker-Polat F., Pinarbasi Degirmenci N., Solaroglu I., and Bagci-Onder T. Tumor cell infiltration into the brain in glioblastoma: from mechanisms to clinical perspectives. *Cancers* **14**, 14020443 (2022).
- Munson, J. M. & Shieh, A. C. Interstitial fluid flow in cancer: implications for disease progression and treatment. *Cancer Manag. Res.* **6**, 317–328 (2014).
- Kingsmore, K. M. et al. MRI analysis to map interstitial flow in the brain tumor microenvironment. *APL Bioeng.* **2**, 031905 (2018).
- Munson, J. M., Bellamkonda, R. V. & Swartz, M. A. Interstitial flow in a 3D microenvironment increases glioma invasion by a CXCR4-dependent mechanism. *Cancer Res.* **73**, 1536–1546 (2013).
- Cornelison, R. C., Brennan, C. E., Kingsmore, K. M. & Munson, J. M. Convective forces increase CXCR4-dependent glioblastoma cell invasion in GL261 murine model. *Sci. Rep.* **8**, 17057 (2018).
- Zhang, J. et al. Clinical applications of contrast-enhanced perfusion mri techniques in gliomas: recent advances and current challenges. *Contrast Media Mol. Imaging* **2017**, 7064120 (2017).
- Carman-Esparza, C. et al. A novel methodology for mapping interstitial fluid dynamics in murine brain tumors using DCE-MRI. *Methods* **231**, 78–93 (2024).
- Kingsmore, K. M. et al. Interstitial flow differentially increases patient-derived glioblastoma stem cell invasion via CXCR4, CXCL12, and CD44-mediated mechanisms. *Integr. Biol.* **8**, 1246–1260 (2016).
- Shieh, A. C. & Swartz, M. A. Regulation of tumor invasion by interstitial fluid flow. *Phys. Biol.* **8**, 015012 (2011).
- Evje, S. & Waldeland, J. O. How Tumor Cells Can Make Use of Interstitial Fluid Flow in a Strategy for Metastasis. *Cell Mol. Bioeng.* **12**, 227–254 (2019).
- Piotrowski-Daspit, A. S., Tien, J. & Nelson, C. M. Interstitial fluid pressure regulates collective invasion in engineered human breast tumors via Snail, vimentin, and E-cadherin. *Integr. Biol.* **8**, 319–331 (2016).
- Polacheck, W. J., Charest, J. L. & Kamm, R. D. Interstitial flow influences direction of tumor cell migration through competing mechanisms. *Proc. Natl. Acad. Sci. USA* **108**, 11115–11120 (2011).
- Qazi, H., Shi, Z.-D. & Tarbell, J. M. Fluid shear stress regulates the invasive potential of glioma cells via modulation of migratory activity and matrix metalloproteinase expression. *PLoS One* **6**, e20348 (2011). vol.no. 5May.
- Qazi, H., Palomino, R., Shi, Z.-D., Munn, L. L. & Tarbell, J. M. Cancer cell glycocalyx mediates mechanotransduction and flow-regulated invasion. *Integr. Biol.* **5**, 1334–1343 (2013).
- Fleury, M. E., Boardman, K. C. & Swartz, M. A. Autologous morphogen gradients by subtle interstitial flow and matrix interactions. *Biophys. J.* **91**, 113–121 (2006).
- Stine C. A. & Munson J. M. Autologous gradient formation under differential interstitial fluid flow environments *Biophysica* **2**, 2010003 (2022).
- Zhao, J., Salmon, H. & Samtinoranont, M. Effect of heterogeneous vasculature on interstitial transport within a solid tumor. *Microvasc. Res.* **73**, 224–236 (2007).
- Elmghirbi, R. et al. Toward a noninvasive estimate of interstitial fluid pressure by dynamic contrast-enhanced MRI in a rat model of cerebral tumor. *Magn. Reson. Med.* **80**, 2040–2052 (2018).
- Baxter, L. T. & Jain, R. K. Transport of fluid and macromolecules in tumors. I. Role of interstitial pressure and convection. *Microvasc. Res.* **37**, 77–104 (1989).
- Tufto, I. & Rofstad, E. K. Interstitial fluid pressure, fraction of necrotic tumor tissue, and tumor cell density in human melanoma xenografts. *Acta Oncol.* **37**, 291–297 (1998).
- Rechichi, G. et al. Endometrial cancer: correlation of apparent diffusion coefficient with tumor grade, depth of myometrial invasion, and presence of lymph node metastases. *AJR Am. J. Roentgenol.* **197**, 256–262 (2011).
- Mori, N. et al. Peritumoral apparent diffusion coefficients for prediction of lymphovascular invasion in clinically node-negative invasive breast cancer. *Eur. Radio.* **26**, 331–339 (2016).
- Yang, W. et al. Minimum apparent diffusion coefficient for predicting lymphovascular invasion in invasive cervical cancer. *J. Magn. Reson. Imaging* **45**, 1771–1779 (2017).
- Pauleit, D. et al. Can the apparent diffusion coefficient be used as a noninvasive parameter to distinguish tumor tissue from peritumoral tissue in cerebral gliomas? *J. Magn. Reson Imaging* **20**, 758–764 (2004).
- Chang, P. D., Chow, D. S., Yang, P. H., Filippi, C. G. & Lignelli, A. Predicting glioblastoma recurrence by early changes in the apparent diffusion coefficient value and signal intensity on FLAIR images. *AJR Am. J. Roentgenol.* **208**, 57–65 (2017).
- Stylianopoulos, T. et al. Diffusion of particles in the extracellular matrix: the effect of repulsive electrostatic interactions. *Biophys. J.* **99**, 1342–1349 (2010).

28. He, X. et al. Extracellular matrix physical properties govern the diffusion of nanoparticles in tumor microenvironment. *Proc. Natl. Acad. Sci. USA* **120**, e2209260120 (2023).
29. Yuan, Z. et al. Extracellular matrix remodeling in tumor progression and immune escape: from mechanisms to treatments. *Mol. Cancer* **22**, 48 (2023).
30. Magdoo, K. N. et al. MRI of whole rat brain perivascular network reveals role for ventricles in brain waste clearance. *Sci. Rep.* **9**, 11480 (2019).
31. Yoshida, T., Matsuda, Y., Naito, Z. & Ishiwata, T. CD44 in human glioma correlates with histopathological grade and cell migration. *Pathol. Int* **62**, 463–470 (2012).
32. Ehteshami, M., Stevenson, C. B. & Thompson, R. C. Preferential expression of chemokine receptor CXCR4 by highly malignant human gliomas and its association with poor patient survival. *Neurosurgery* **63**, E820 (2008).
33. Wang S. et al. The CXCL12/CXCR4 axis confers temozolomide resistance to human glioblastoma cells via up-regulation of FOXM1. *J. Neurol. Sci.* **414**, 116837 (2020).
34. Verhaak, R. G. W. et al. Integrated Genomic Analysis Identifies Clinically Relevant Subtypes of Glioblastoma Characterized by Abnormalities in PDGFRA, IDH1, EGFR, and NF1. *Cancer Cell* **17**, 98–110 (2010).
35. Pietras, A. et al. Osteopontin-CD44 signaling in the glioma perivascular niche enhances cancer stem cell phenotypes and promotes aggressive tumor growth. *Cell Stem Cell* **14**, 357–369 (2014).
36. Johansson, E. et al. CD44 interacts with HIF-2 α to modulate the hypoxic phenotype of perinecrotic and perivascular glioma cells. *Cell Rep.* **20**, 1641–1653 (2017).
37. “CD44 as a prognostic and predictive marker for GBM. | J. Clin. Oncol.” Accessed: May 22, 2025. [Online]. Available: https://ascopubs.org/doi/10.1200/jco.2011.29.15_suppl.2049.
38. Lemasson, B. et al. Impact of perfusion map analysis on early survival prediction accuracy in glioma patients. *Transl. Oncol.* **6**, 766 (2013).
39. Díez Valle, R. et al. Surgery guided by 5-aminolevulinic fluorescence in glioblastoma: volumetric analysis of extent of resection in single-center experience. *J. Neurooncol* **102**, 105–113 (2011).
40. Alvarez, N. & Sevilla, A. Current advances in photodynamic therapy (PDT) and the future potential of PDT-combinatorial cancer therapies. *Int J. Mol. Sci.* **25**, 1023 (2024).
41. Beck, T. J. et al. Interstitial photodynamic therapy of nonresectable malignant glioma recurrences using 5-aminolevulinic acid induced protoporphyrin IX. *Lasers Surg. Med.* **39**, 386–393 (2007).
42. Jensen, T. R. & Schmainda, K. M. Computer-aided detection of brain tumor invasion using multiparametric MRI. *J. Magn. Reson. Imaging* **30**, 481–489 (2009).
43. Zhang, F. et al. In vivo MRI tracking of cell invasion and migration in a rat glioma model. *Mol. Imaging Biol.* **13**, 695–701 (2011).
44. Juvekar, P. et al. ReMIND: the brain resection multimodal imaging database. *Sci. Data* **11**, 494 (2024).
45. Revilla-Pacheco, F. et al. Extent of resection and survival in patients with glioblastoma multiforme: Systematic review and meta-analysis. *Medicine* **100**, e26432 (2021).
46. Ellingson, B. M., Wen, P. Y. & Cloughesy, T. F. Evidence and context of use for contrast enhancement as a surrogate of disease burden and treatment response in malignant glioma. *Neuro Oncol.* **20**, 457–471 (2018).
47. Krauze, A. V. et al. Glioblastoma survival is associated with distinct proteomic alteration signatures post chemoradiation in a large-scale proteomic panel. *Front Oncol.* **13**, 1127645 (2023).
48. Awad, A.-W. et al. Impact of removed tumor volume and location on patient outcome in glioblastoma. *J. Neurooncol.* **135**, 161–171 (2017).
49. Lim, H., Albatany, M., Martínez-Santesteban, F., Bartha, R. & Scholl, T. J. Longitudinal measurements of intra- and extracellular pH gradient in a rat model of glioma. *Tomography* **4**, 46–54 (2018).
50. Pak, E. et al. Prediction of prognosis in glioblastoma using radiomics features of dynamic contrast-enhanced MRI. *Korean J. Radio.* **22**, 1514–1524 (2021).
51. Zhang, N. et al. Correlation of volume transfer coefficient K_{trans} with histopathologic grades of gliomas. *J. Magn. Reson Imaging* **36**, 355–363 (2012).
52. De Fazio, E. et al. Intrinsic and microenvironmental drivers of glioblastoma invasion. *Int J. Mol. Sci.* **25**, 2563 (2024).
53. Lee, J. et al. Tumor stem cells derived from glioblastomas cultured in bFGF and EGF more closely mirror the phenotype and genotype of primary tumors than do serum-cultured cell lines. *Cancer Cell* **9**, 391–403 (2006).
54. Sanna, M. G. et al. Bitopic sphingosine 1-phosphate receptor 3 (S1P3) antagonist rescue from complete heart block: pharmacological and genetic evidence for direct S1P3 regulation of mouse cardiac conduction. *Mol. Pharm.* **89**, 176–186 (2016).

Acknowledgements

The authors would like to thank Maosen Wang, Jack Roy, and Jeremy Gatesman for assistance with MRI, Samantha Haynes, Ehab Saleem, Micaiah Lee, and Skylar Davis, for assistance with MRI image analysis and tissue sectioning. This work was funded by NCI R37CA222563 to JMM, the RedGates Foundation to JMM (Virginia Tech), American Cancer Society Institutional Research Grant to JMM (UVA), and NINDS R01NS115971 to RCR and JMM, NSF GRFP to KMK and CME.

Author contributions

Author contributions: Conceptualization: J.M.M., C.M.E., C.A.S., N.A., and J.J.C. Data curation: J.J.C. Methodology: C.M.E., C.A.S., N.A., K.M.K., M.W., J.J.C., and J.M.M. Formal analysis: C.M.E., J.J.C., C.A.S., and N.A. Investigation: C.M.E., C.A.S., K.M.K., M.W., N.A., J.J.C., and J.M.M. Visualization: C.M.E., C.A.S., N.A., J.J.C., and J.M.M. Funding acquisition: J.M.M., R.C.R., K.M.K., and C.M.E. Project administration: J.J.C. and J.M.M. Resources: J.M.M. Software development: J.J.C. Supervision: J.J.C., J.M.M., and R.C.R. Visualizations: C.M.E., J.J.C., C.A.S., N.A., and J.M.M. Writing – original draft: C.M.E., C.A.S., N.A., J.J.C., and J.M.M. Writing – review & editing: C.M.E., C.A.S., N.A., K.M.K., M.W., R.T.W., R.C.R., J.J.C., and J.M.M.

Competing interests

Drs. Munson, Rockne, Stine, Cunningham, and Woodall are co-founders in Cairina, Inc, a company based in part on some of the methods described herein.

Additional information

Supplementary information The online version contains supplementary material available at <https://doi.org/10.1038/s44385-025-00033-x>.

Correspondence and requests for materials should be addressed to Jessica J. Cunningham or Jennifer M. Munson.

Reprints and permissions information is available at <http://www.nature.com/reprints>

Publisher's note Springer Nature remains neutral with regard to jurisdictional claims in published maps and institutional affiliations.

Open Access This article is licensed under a Creative Commons Attribution-NonCommercial-NoDerivatives 4.0 International License, which permits any non-commercial use, sharing, distribution and reproduction in any medium or format, as long as you give appropriate credit to the original author(s) and the source, provide a link to the Creative Commons licence, and indicate if you modified the licensed material. You do not have permission under this licence to share adapted material derived from this article or parts of it. The images or other third party material in this article are included in the article's Creative Commons licence, unless indicated otherwise in a credit line to the material. If material is not included in the article's Creative Commons licence and your intended use is not permitted by statutory regulation or exceeds the permitted use, you will need to obtain permission directly from the copyright holder. To view a copy of this licence, visit <http://creativecommons.org/licenses/by-nc-nd/4.0/>.

© The Author(s) 2025